

Magnetic transitions of biphenylene network layers induced by external perturbations

Sejoong Kim^{1,2,*}

¹*University of Science and Technology (UST), Gajeong-ro 217, Daejeon 34113, Korea*

²*Korea Institute for Advanced Study, Hoegiro 85, Seoul 02455, Korea*

(Dated: February 21, 2024)

We present a comprehensive investigation of the magnetic ordering in biphenylene network (BPN) layers, employing density functional theory (DFT) calculations under external perturbations, including uniaxial strains and hole doping. We compute fully relaxed structures, energy bands, and magnetic states by performing DFT calculations augmented with extended Hubbard interactions, encompassing both on-site and inter-site interactions, to accurately capture electron correlations. We emphasize the importance of the extended Hubbard forces by contrasting BPN layers with and without the forces. Our results reveal that in their fully relaxed structures, both BPN monolayer and bilayer are non-magnetic. We exploit external perturbations to induce magnetic ordering. The application of uniaxial strains induces magnetic phase transitions, leading to ferrimagnetic and antiferromagnetic states in BPN monolayer and bilayer, respectively. Additionally, we investigate hole doping as an alternative mechanism for inducing magnetic transitions. Our findings shed light on the tunability of magnetic properties in BPN layers through external perturbations, demonstrating the promise of low-dimensional materials in future spintronics and nanoelectronic applications.

I. INTRODUCTION

Recently a new planar carbon allotrope has been experimentally synthesized on the Au(111) surface throughout a bottom-up process¹. The carbon allotrope is called biphenylene network (BPN), which consists of octagon, hexagon, and tetragon rings of sp^2 -hybridized carbon atoms. In the experiment BPN was grown as an armchair-edged nanoribbon structure whose width is up to 18 carbon atoms, but it is certainly expected to realize a large-scale two-dimensional BPN single-layer in the future. It would serve as a versatile platform to investigate fundamental physics of condensed matter systems as graphene has done so far².

The experimental realization of BPN layers has sparked significant interests in exploring their electronic, phononic, mechanical, chemical, and thermal properties³⁻³⁸. Recent studies^{3,4} have revealed that the 2D BPN lattice exhibits intriguing electronic band structures such as type-II Dirac cones³⁹, nearly flat bands, and saddle-point van Hove singularities (vHS). These characteristics are closely related to topological and correlation physics. It is confirmed that the 2D BPN lattice constitutes a \mathbb{Z}_2 topological material, hosting topologically protected boundary states^{3,4}. Furthermore, the presence of saddle point vHS and nearly flat bands provide enhanced density of states (DOS), implying the potential emergence of correlation-related physics in the 2D BPN lattice. In this context, the possibility of magnetic ordering in a pristine 2D BPN monolayer has been investigated using the density functional theory (DFT) calculations³. It is known that magnetic ordering can be induced through edge geometry modifications⁴⁰⁻⁴², defect introduction^{43,44}, hydrogenation⁴⁵⁻⁴⁷, and adatom incorporation⁴⁸ in carbon materials like graphene, but the presence of magnetism in pristine carbon materials is rare⁴⁹. The 2D BPN lattice can be a promising candidate for magnetic all-carbon materials. Understanding mag-

netic ordering in BPN layers is crucial for their potential application as future spintronics platforms¹⁷.

To understand correlation physics such as magnetism, it is of vital importance to consider many-body electron interactions in DFT calculations. To incorporate many-body electron correlations into DFT calculations, it is required to use advanced methods going beyond the mean-field level of the conventional correlation-exchange functionals such as the local density approximation (LDA) and the generalized gradient approximation (GGA). Correlation physics such as magnetic phase transitions can be investigated through the use of a newly developed DFT+ U + V method⁵⁰⁻⁵⁵. The DFT+ U + V method includes not only on-site Hubbard interactions (U), but also inter-site interactions (V), thereby capturing the intricate interplay between strong electron localization and hybridization of extended neighboring orbitals, particularly for systems featuring covalent bonding characters. Remarkably, this extended Hubbard approach has demonstrated its capability to capture the effect of Coulomb interactions in electronic structure calculations at the similar level of GW approximations⁵⁶, with applications spanning not only three-dimensional solids^{50,51,54,55}, but also low-dimensional materials such as graphene⁵⁵ and black phosphorus⁵⁴.

When investigating possible magnetic ordering of BPN layers, one crucial consideration is accurate estimation of atomic structures. Influenced by atomic structure details, the positions of saddle-point vHS and nearly flat bands with respect to the Fermi energy E_F are determined. To this end, accurate atomic structure predictions for BPN layers are imperative, considering electron correlations within the DFT+ U + V method. Regarding the potential impact of extended Hubbard corrections in introducing additional forces, it is possible that lattice constants and atomic configurations may deviate from those predicted by the mean-field level of DFT calculations. Noteworthy advancements have recently focused

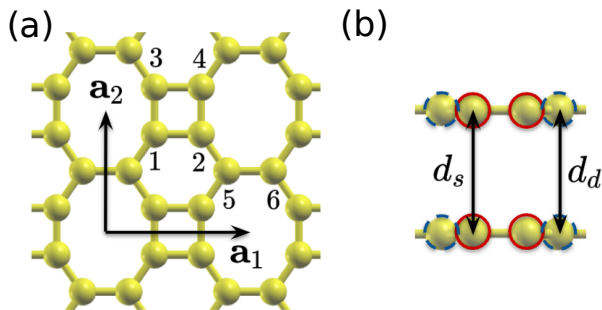


FIG. 1. (Color online) (a) In-plane atomic configuration of BPN lattice. Carbon atoms are numbered from 1 to 6. Atoms from 1 to 4 belong to the square cluster, while atoms 5 and 6 constitute the dimer part. Lattice vectors $\mathbf{a}_1 = a_1\hat{x}$ and $\mathbf{a}_2 = a_2\hat{y}$ are indicated. (b) Side view of bilayer BPN. Atoms belonging to square cluster and dimer are surrounded by red solid lines and blue dashed ones. Inter-layer distances between square clusters (dimers) are denoted by d_s (d_d). Atomic configurations are drawn by using XCrySDen⁶⁰.

on forces corrected by extended Hubbard terms, enabling successful calculations of lattice dynamics with extended Hubbard interactions^{57–59}. The force calculation scheme, encompassing extended Hubbard forces, can be readily used to obtain fully relaxed atomic structures within the DFT+ U + V calculations.

In this study, we conducted a comprehensive investigation into magnetic transitions of BPN layers by the DFT+ U + V method. We undertook the relaxation of atomic structures for BPN monolayer and bilayer, employing the extended Hubbard forces. By analyzing the positions of vHS and flat bands relative to E_F , we contrasted the electronic structures and magnetic ordering of BPN layers with and without the extended Hubbard forces. We showed that the subtle modification of the atomic structure due to the extended Hubbard forces predicts a non-magnetic state unlike the previous study³. Subsequently, we explored their magnetic properties by subjecting them to external perturbations such as uniaxial strains and doping.

II. COMPUTATIONAL DETAILS

For DFT calculations we use QUANTUM ESPRESSO^{61,62} with the plane-wave (PW) basis, the PBE exchange-correlation functional⁶³ and norm-conserving pseudopotentials^{64,65}. We also use a van der Waals (vdW) correction known as rev-vdW-DF2^{66,67}. We adopt $16 \times 16 \times 1$ k -point mesh, and the kinetic energy cutoff 100 Ry for self-consistent calculations. To prevent interactions between periodic image layers, a vacuum region with a size of 15 Å is employed. To incorporate many-body electron correlations, we employed the DFT+ U + V method recently implemented in QUANTUM ESPRESSO⁵⁴, where on-site

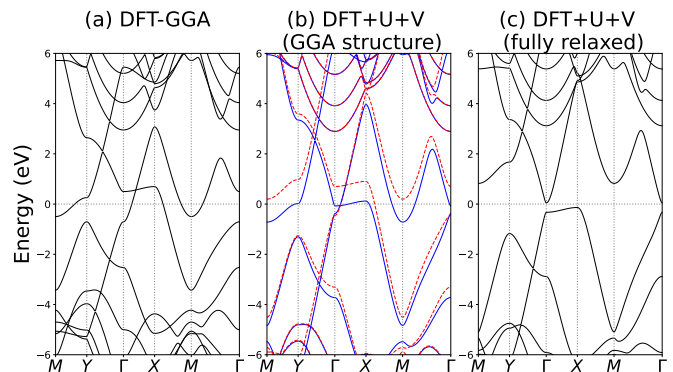


FIG. 2. (Color online) Band structures of monolayer BPN (a) Band structures calculated by DFT-GGA. (b) Band structures computed from the DFT+ U + V method by using the GGA structure (c) Band structures of monolayer BPN fully relaxed by the DFT+ U + V method. Non-magnetic energy bands are indicated by black solid lines. Energy bands of the magnetic state are drawn by blue solid lines and red dashed ones, which correspond to opposite spin orientations. Here E_F is set to be zero.

and inter-site Hubbard interactions are self-consistently determined by using the Hartree-Fock formalism based on the pseudohybrid Hubbard density functional known as ACBN0⁶⁸. All atomic structures are relaxed to ensure that all components of forces acting on atoms are below 0.051 eV/Å. Note that we call conventional DFT calculations with GGA functionals as DFT-GGA in order to distinguish against the DFT+ U + V method.

III. RESULTS AND DISCUSSION

A. Relaxed structures

First we compare the atomic structures of both the BPN monolayer and bilayer, which are relaxed using DFT-GGA calculations as well as the DFT+ U + V method. Figure 1 illustrates the atomic configurations of BPN layers. The BPN lattice layer contains six carbon atoms in the unit cell. As depicted in Fig. 1(a), the carbon atoms are labeled accordingly, with atoms 1 to 4 forming a square cluster, and atoms 5 and 6 forming a dimer. For the monolayer BPN, all six atoms reside within the same plane, without any out-of-plane displacement. The BPN lattice exhibits a pattern consisting of square, hexagon, and octagon rings. Additionally, when stacking BPN layers, each layer precisely aligns on top of its neighboring layer, as demonstrated in Fig. 1(b).

Table I presents a comparison of lattice constants and atomic configurations of BPN lattices, which are relaxed using GGA and DFT+ U + V methods. With the inclusion of U + V corrections, the lattice constant a_1 decreases from 4.52 Å to 4.47 Å, while the lattice constant a_2 increases from 3.77 Å to 3.80 Å. Consequently, the

monolayer	$ \mathbf{a}_1 $	$ \mathbf{a}_2 $	d_{12}	d_{13}	d_{56}	d_{25}	θ_{123}	θ_{234}	θ_{256}		
DFT-GGA	4.52	3.77	1.46	1.46	1.45	1.41	90°	90°	124.9°		
DFT+ $U+V$	4.47	3.80	1.41	1.51	1.46	1.40	90°	90°	124.8°		
bilayer	$ \mathbf{a}_1 $	$ \mathbf{a}_2 $	d_{12}	d_{13}	d_{56}	d_{25}	θ_{123}	θ_{234}	θ_{256}	d_s	d_d
DFT-GGA	4.52	3.77	1.46	1.46	1.45	1.41	90°	90°	124.9°	3.24	3.28
DFT+ $U+V$	4.47	3.81	1.41	1.51	1.47	1.40	90°	90°	124.8°	3.48	3.48

TABLE I. Atomic structure parameters of monolayer and bilayer BPN optimized by DFT-GGA and DFT+ $U+V$ calculations.

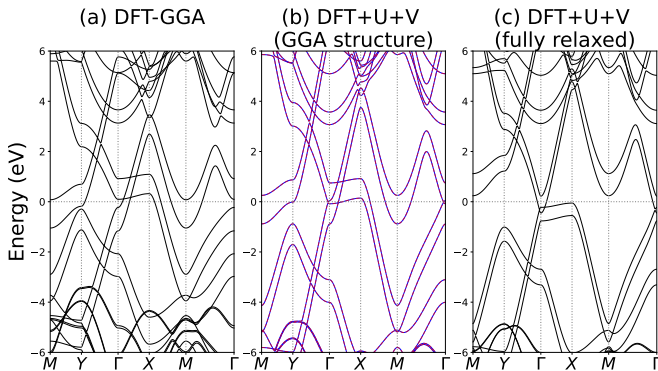


FIG. 3. (Color online) Band structures of bilayer BPN (a) Band structures calculated by DFT-GGA. (b) Band structures computed from the DFT+ $U+V$ method by using the GGA structure (c) Band structures of monolayer BPN fully relaxed by the DFT+ $U+V$ method. Non-magnetic energy bands are indicated by black solid lines. Energy bands of the magnetic state are drawn by blue solid lines and red dashed ones, which correspond to opposite spin orientations.

DFT+ $U+V$ method predicts that a square with DFT-GGA is transformed to the rectangle cluster, experiencing contraction along the x -axis and elongation along the y -axis. Furthermore, the size of the dimer slightly increases by 0.02 Å.

For the BPN bilayer, the energy minimum configuration is the on-top stacking where the upper layer is exactly on the top of the lower layer as shown in Fig. 1. both DFT-GGA and DFT+ $U+V$ calculations indicate the intra-layer configurations remain the same as those of the monolayer. However, the inclusion of $U+V$ corrections leads to changes in inter-layer configurations. In the DFT-GGA calculations, carbon atoms in the bilayer exhibit small out-of-plane displacements. The inter-layer distances between atoms in the square cluster and the dimer, denoted as d_s and d_d respectively, are found to be $d_s = 3.24$ Å and $d_d = 3.28$ Å as indicated in Fig. 1(b) and Table I. When $U+V$ corrections are incorporated, the inter-layer distance undergoes an increase of approximately 0.24 Å, and out-of-place displacements disappear.

B. Band Structures

We observed distinct electronic structure properties of monolayer BPN, predicted by DFT-GGA and DFT+ $U+V$ calculations, as demonstrated in Fig. 2. We reproduced the DFT-GGA electronic band structures as reported Ref.^{3,10}. DFT-GGA calculations reveal a saddle-shaped band hosting the van Hove singularity (vHS) at Γ , intersecting with the nearly flat band around $\frac{2}{5}\Gamma X$ in Fig. 2(a). The band structures in the vicinity of the crossing point exhibit a type-II Dirac state^{39,69–72}. The nearly flat band is mainly composed of p_z orbitals localized on the square cluster. The saddle-shaped band is formed by the combination of p_z orbitals on the square unit and the dimer, with the main contribution coming from p_z orbitals of the dimer. An additional remarkable feature of the band structure is the presence of a saddle-shaped band that hosts another vHS near the Y point around E_F .

Next we perform DFT+ $U+V$ calculations using the atomic structure relaxed by DFT-GGA, in order to differentiate them from the full DFT+ $U+V$ calculations where atomic structures are entirely relaxed using $U+V$ corrections. Here we call the atomic structures relaxed by DFT-GGA as GGA structures. The self-consistent calculations of onsite (U) and inter-site (V) Hubbard interactions are $U_t = 5.96$ eV, $U_d = 6.01$ eV, $V_{12} = V_{34} = V_{13} = V_{24} = 3.06$ eV, $V_{56} = 3.11$ eV, and $V_{25} = 3.14$ eV, where t and d denote the tetragon and the dimer respectively and atomic site numbers in inter-site interactions follow Fig. 1(a). In comparison with DFT-GGA calculations, the inclusion of $U+V$ corrections leads to increased overall bandwidths of the resulting band structures. The DFT+ $U+V$ calculations with GGA structures reveal a ferrimagnetic ground state for the single-layer BPN, where the square unit and the dimer possess opposite magnetic moments. For example, Fig. 10(a) represents spin polarization density $\Delta\rho \equiv \rho_\uparrow - \rho_\downarrow$ of the ferrimagnetic phase, where ρ_\uparrow and ρ_\downarrow are spin-up and spin-down densities, respectively. Since their magnetic moments do not completely cancel out, monolayer BPN exhibits a net magnetic moment. Figure 2(b) illustrates the spin-resolved band structures of the ferrimagnetic ground state, displaying opposite spin orientations. In comparison to DFT-GGA band structures, vHS moves closer to E_F , and one nearly flat band at ΓX shifts downwards towards E_F . Accordingly, among four

crossing points between two saddle-shaped bands and two nearly flat bands, two of them are located in the vicinity of Γ -point and have energies close to E_F .

However, when the atomic structure is fully relaxed with the DFT+ U + V method, the corresponding band structures exhibit different electronic properties compared to DFT+ U + V calculations with GGA structures. Firstly, the resulting ground state is non-magnetic, which is in contrast to the fact that the DFT+ U + V calculations with GGA structures predict a ferrimagnetic ordering. Secondly, as illustrated in Fig. 2(c), a band gap opens at the zone center even in the fully relaxed structure without external perturbations such as strains and doping. It is found that the band edge minimum at M moves upward above E_F , resulting in the single layer BPN being a semiconductor with an indirect band gap between the conduction band bottom at Γ and the valence band top at X . We also note that the self-consistent Hubbard interactions for the full DFT+ U + V calculation are $U_t = 5.99$ eV, $U_d = 6.00$ eV, $V_{12} = V_{34} = 3.14$ eV, $V_{13} = V_{24} = 3.00$ eV, $V_{56} = 3.07$ eV, and $V_{25} = 3.15$ eV.

We extend our discussions to electronic band structures of bilayer BPN, comparing DFT-GGA calculations and DFT+ U + V ones. In the DFT-GGA calculations, bilayer BPN is found to be non-magnetic. The resulting band structures, as shown in Fig. 3(a), exhibit two nearly flat bands along ΓX direction and two bands hosting vHS at the Γ point. These bands intersect at four points along ΓX .

Using atomic structures relaxed by DFT-GGA (GGA structures), DFT+ U + V calculations reveal that bilayer BPN exhibits an antiferromagnetic ground state. Each layer displays a ferrimagnetic order similar to monolayer BPN in the same calculation condition, but the upper and lower layers possess opposite spin orientations. The self-consistent evaluations of Hubbard interactions are $U_t = 5.98$ eV, $U_d = 6.02$ eV, $V_{12} = V_{34} = V_{13} = V_{24} = 3.06$ eV, $V_{56} = 3.11$ eV, and $V_{25} = 3.14$ eV, which are almost the same with those of monolayer BPN in DFT+ U + V calculations with GGA structure. The band structures from DFT+ U + V calculations using the GGA structures, as depicted in Fig. 3(b), show each band to be doubly degenerate with opposite spin configurations. The crossing point between the upper band with vHS and the lower flat band is annihilated with its time-reversal partner at Γ , so there are three type-II Dirac points.

Fully relaxed the atomic configuration with the DFT+ U + V method, the bilayer BPN reverts to a non-magnetic state. In Fig. 3(c), all type-II Dirac points merge with their time-reversal partners, leaving no type-II Dirac point remaining. Around E_F , there are two V-shaped bands on the conduction side and two trapezoid-shaped valence bands, which include flat bands on ΓX . Unlike monolayer BPN, the bilayer BPN is metallic due to overlap between lower V-shaped band and upper flat band around E_F . Note that the self-consistent Hubbard interactions for the full DFT+ U + V calculation for bilayer BPN are the same with those of monolayer BPN.

We also consider electronic structures of other stacking configurations as well as the energy-minimum on-top configuration. We shift the x and y positions of the upper layer relative to the lower layer by Δx and Δy . Depending on Δx and Δy , it is found that bilayer BPN can be either metal or semiconductor, whose band gap is about from 10 meV to 200 meV as shown in Fig. 4(a). Regardless of stacking configurations, bilayer BPN remains non-magnetic.

C. Magnetic transitions

It is shown that monolayer and bilayer BPN fully relaxed within the DFT+ U + V method are non-magnetic, which is in contrast to the fact that monolayer and bilayer BPN exhibit magnetic ordering when the DFT+ U + V method is employed with GGA structures. The key distinction arises from the relative positions of intriguing electronic structures such as nearly flat bands and saddle-point vHS with respect to E_F . This observation suggests a strategy to induce magnetic ordering in BPN layers: Tuning positions of nearly flat bands and saddle-point vHS, which can be achieved through external perturbations like uniaxial strains and hole doping.

1. Uniaxial strains

We investigate the impact of uniaxial strains on the magnetic transitions of monolayer and bilayer BPN. External strains cause shifts in the positions of vHS and flat bands relative to E_F , potentially leading to magnetic transitions. We observed that the GGA structure, which possesses a larger lattice constant a_1 than the DFT+ U + V structure, exhibits magnetism with the U + V correction. This observation suggests that enlarging the unit cell may induce a magnetic transition.

Figures 5(a) and (b) present total and absolute magnetization as a function of ε_{yy} and ε_{xx} , respectively. Here the uniaxial strain ε_{xx} (ε_{yy}) along x (y) direction is expressed as $(a_1 - a_1^0)/a_1^0$ ($(a_2 - a_2^0)/a_2^0$), where a_1^0 and a_2^0 represent the lattice constants along x and y directions without external strains, respectively, as summarized in Table. I. When uniaxial y -strains are applied, we find that they do not induce a magnetic transition. For example, as shown in Fig. 5(c), the band structures at $\varepsilon_{yy} = 2.89\%$ demonstrate that uniaxial y strains lead to an enhancement of the band gap opening around E_F , resulting in a lack of DOS involved in the magnetic transition.

In contrast, uniaxial strains along x direction can trigger a transition from a non-magnetic state to a ferrimagnetic one. The magnetic transition to a ferrimagnetic phase is observed at $\varepsilon_{xx} \approx 4.90\%$. For smaller ε_{xx} , type-II Dirac points are annihilated with vHS, leading to the opening of an energy gap at Γ . For example, at $\varepsilon_{xx} = 3.80$ in Fig. 5(d), a small energy gap is observed at Γ . However, as ε_{xx} increases above 4.90%, Dirac points

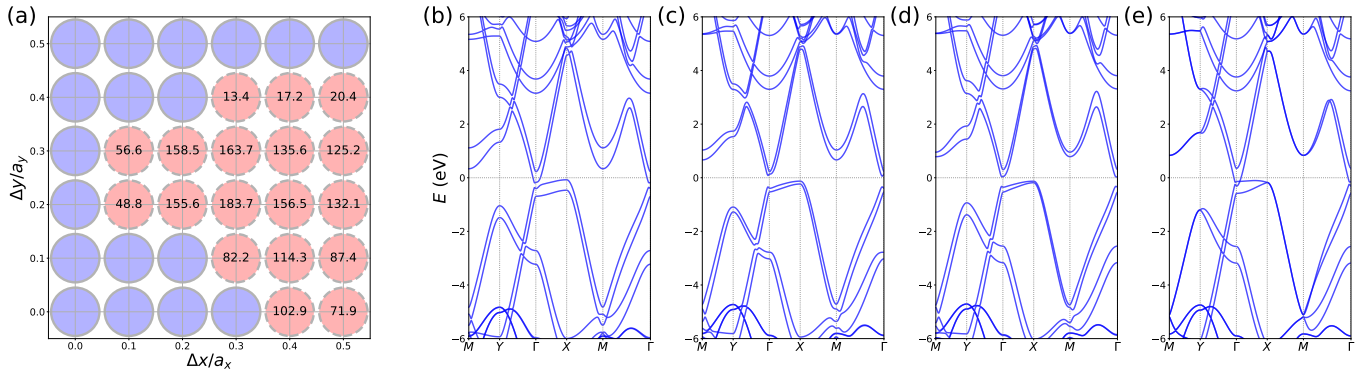


FIG. 4. (Color online) Electronic structures of stacking configurations for bilayer BPBs: (a) Band gaps depending on Δx and Δy . Blue circles with solid edge lines (red circles with dashed edge lines) represent that the corresponding stacking configuration is metal (semiconductor). For semiconducting configurations, band gap energy is written inside the circle in a unit of meV. Band structures for (a) $\Delta x/a_x = 0.1$ and $\Delta y/a_y = 0.1$, (b) $\Delta x/a_x = 0.3$ and $\Delta y/a_y = 0.2$, (c) $\Delta x/a_x = 0.4$ and $\Delta y/a_y = 0.2$, and (d) $\Delta x/a_x = 0.5$ and $\Delta y/a_y = 0.5$. Here E_F is set to be zero.

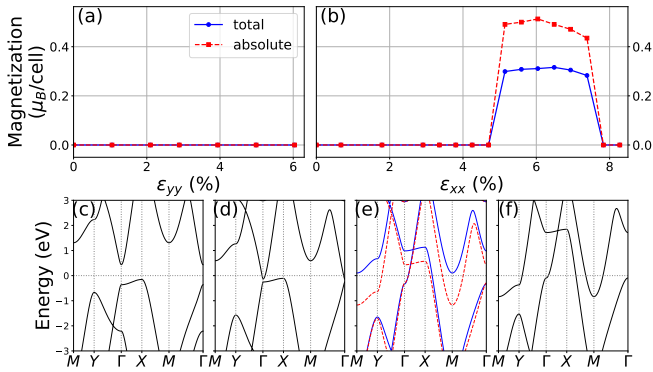


FIG. 5. (Color online) Magnetization of single-layer BPN as a function of uniaxial strains (a) ε_{yy} and (b) ε_{xx} . Absolute and total magnetizations are denoted by red dashed lines with square markers and blue solid lines with closed circle markers, respectively. Band structures with uniaxial strains (c) $\varepsilon_{yy} = 2.89$ ($a_2 = 3.92$) (d) $\varepsilon_{xx} = 3.80$ ($a_1 = 4.64$) (e) $\varepsilon_{xx} = 6.04$ ($a_1 = 4.74$) (f) $\varepsilon_{xx} = 8.28$ ($a_1 = 4.84$). Strains and lattice constants are in unit of % and \AA , respectively. Black solid lines indicate non-magnetic energy bands. Energy bands of the magnetic state are drawn by blue solid lines and red dashed ones, which correspond to opposite spin orientations. Here E_F is set to be zero.

and vHS reappear around E_F , causing the energy gap at Γ to close. At the same time, vHS at Y and the conduction band edge at M move downward to E_F .

The ferrimagnetic phase, characterized by total magnetization being smaller than absolute one, persists up to $\varepsilon_{xx} \approx 7.60$ % as shown in Fig. 5(b). For the ferrimagnetic phase, energy bands associated with opposite spin orientations are lifted, for example, as illustrated in Fig 5(b) for $\varepsilon_{xx} \approx 6.04$ %. Beyond the strain level $\varepsilon_{xx} \approx 7.60$ %, the single-layer BPN returns to a non-magnetic state. At x strains higher than 7.60 %, the two vHS points at Γ

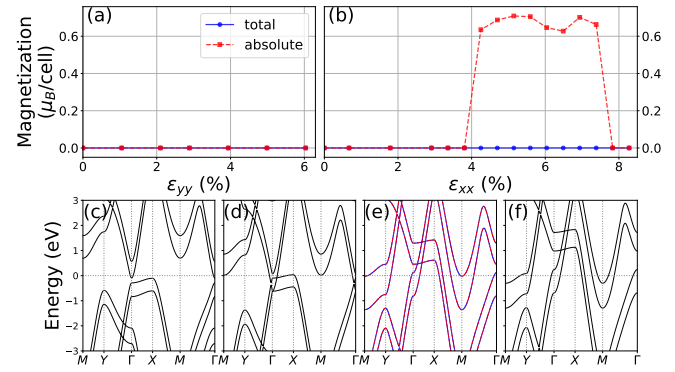


FIG. 6. (Color online) Magnetization of bilayer BPN as a function of uniaxial strains (a) ε_{yy} and (b) ε_{xx} . Absolute and total magnetizations are denoted by red dashed lines with square markers and blue solid lines with closed circle markers, respectively. Band structures with uniaxial strains (c) $\varepsilon_{yy} = 2.89$ ($a_2 = 3.92$) (d) $\varepsilon_{xx} = 3.36$ ($a_1 = 4.62$) (e) $\varepsilon_{xx} = 6.04$ ($a_1 = 4.74$) (f) $\varepsilon_{xx} = 7.83$ ($a_1 = 4.82$). Strains and lattice constants are in unit of % and \AA , respectively. Black solid lines indicate non-magnetic energy bands. Energy bands of the magnetic state are drawn by blue solid lines and red dashed ones, which correspond to opposite spin orientations. Here E_F is set to be zero.

and Y are located near E_F , while the flat band on ΓX moves further away from E_F . For example, see Fig. 5(f).

Under uniaxial strains, bilayer BPN undergoes magnetic transitions similar to the single-layer case. uniaxial y strains eliminate the small overlap between the lower V-shaped band and the upper flat band present in the fully relaxed structure, eventually leading to a semiconducting state with an indirect band gap. See Fig. 6(c). No magnetic transition is observed as the DOS vanishes around E_F .

Under the application of uniaxial x strains, the bilayer

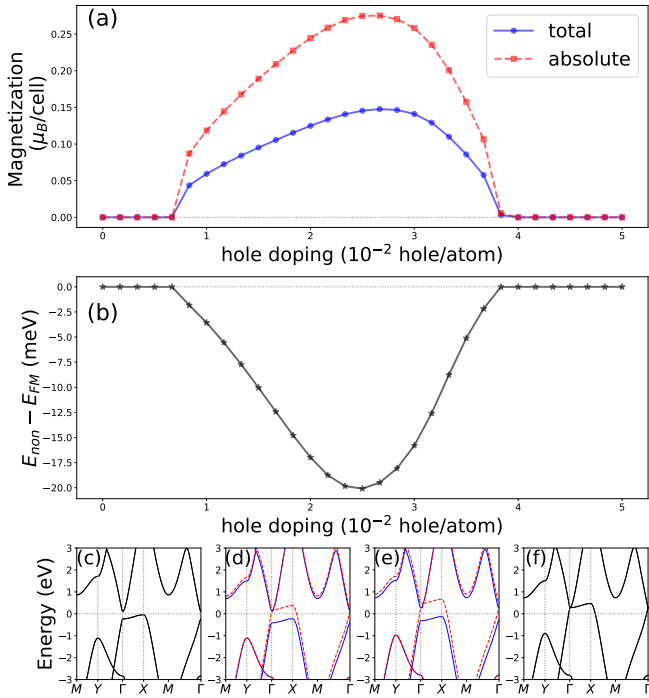


FIG. 7. (Color online) (a) Magnetization of single-layer BPN as a function of hole doping concentration. Red dashed lines with square markers (blue solid lines with close circles) denote absolute (total) magnetization. (b) Total energy differences between non-magnetic and magnetic phases. Band structures at hole doping concentrations (c) 0.33 (d) 1.67 (e) 2.50 (f) 4.17 in unit of 10^{-2} hole per atom. Black solid lines indicate non-magnetic energy bands. Energy bands of the magnetic state are drawn by blue solid lines and red dashed ones, which correspond to opposite spin orientations. Here E_F is set to be zero.

BPN undergoes an antiferromagnetic transition, where the upper and lower layers have opposite spin orientations, resulting in the absence of total magnetization, for example, as shown in Fig. 10(b). The magnetic transition takes place at $\varepsilon_{xx} \approx 4.0\%$, which is smaller than the transition strain observed for the monolayer BPN. When $\varepsilon_{xx} < 4.0\%$, at which bilayer BPN is non-magnetic, some of type-II Dirac points and vHS around Γ are partly restored, as illustrated in Fig. 6(d) where $\varepsilon_{xx} < 3.36\%$. Around the transition strain $\varepsilon_{xx} \approx 4.0$, all four crossing points between two flat bands and two saddle-shaped bands are fully recovered. For $\varepsilon_{xx} > 4.00\%$, the bilayer BPN becomes antiferromagnetic, and this antiferromagnetic ordering persists up to $\varepsilon_{xx} \approx 7.6$. We also note that the two flat bands on ΓX shift upward, and the conduction bands around M and Y move down, as ε_{xx} increases.

Note that we also consider other mechanical perturbations such as biaxial strains and in-plane and out-of-plane hydrostatic pressure. Applying biaxial strains up to 10% and in-plane hydrostatic pressure (up to 10% lattice

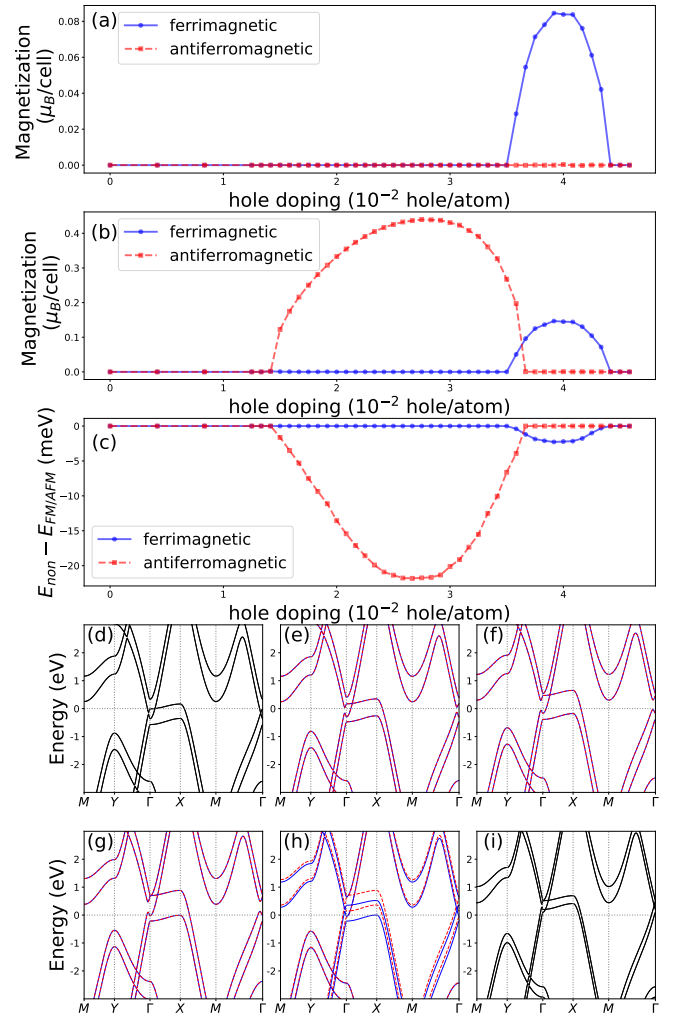


FIG. 8. (Color online) (a) Total magnetization of bilayer BPN as a function of hole doping concentration. (a) Absolute magnetization of bilayer BPN as a function of hole doping concentration. (c) Total energy differences between non-magnetic and magnetic phases. Red dashed lines with square markers (blue solid lines with close circles) denote the total magnetization of the antiferromagnetic state (ferrimagnetic state) for (a), (b), and (c). Band structures of bilayer BPN at hole doping concentrations (d) 0.83 (e) 1.67 (f) 2.50 (g) 3.33 (h) 3.75 (i) 4.58 in a unit of 10^{-2} hole/atom. Black solid lines indicate non-magnetic energy bands. Energy bands of the magnetic state are drawn by blue solid lines and red dashed ones, which correspond to opposite spin orientations. Here E_F is set to be zero.

shrinkage), we do not observe magnetic transitions. Using out-of-plane hydrostatic pressure on bilayer BPN, we find no magnetic transition with interlayer distance reduction up to 1.6 Å.

2. Hole doping

Considering that flat bands on ΓX are below E_F [Figs. 2(c) and 3(c)], hole doping might induce magnetic transitions by aligning the flat bands around E_F . To investigate this scenario, we performed DFT+ U + V calculations with different hole doping concentrations in single-layer and bilayer BPN, as shown in Figs. 7 and 8.

Figure 7(a) presents that single-layer BPN becomes ferrimagnetic at a hole doping concentration $n_h \approx 7 \times 10^{-3}$ hole per atom. In the ferrimagnetic phase, spins of rectangle clusters and dimers are oriented in opposite directions, similar to the ferrimagnetic ordering induced by uniaxial strains. The ferrimagnetic ordering is maintained up to about $n_h \approx 3.8 \times 10^{-2}$ hole per atom.

The band structures near E_F show different evolutions for hole doping, compared to uniaxial strains. In the case of uniaxial strains, the ferrimagnetic phase transition is typically accompanied by the full restoration of type-II Dirac points and vHS around Γ , as shown in the previous section. However, the ferrimagnetic state induced by hole doping has different band structures around E_F depending on spin orientations. For example, as shown in Fig. 7(d), the energy bands associated with one spin direction exhibit a saddle point at Γ and Dirac points with the flat band on ΓX located above E_F . Conversely, no Dirac point or vHS are recovered in the band structures with the opposite spin orientation. Additionally, it is worth noting that overall band structures, including the other vHS at Y and conduction band edges at M , move upwards relative to E_F as hole doping concentrations increase. This is in contrast to the case of uniaxial strains, where band structures around YM evolve in the opposite direction compared with those on ΓX .

Hole doping also induces magnetic transitions in bilayer BPN, as illustrated in Fig. 8. The critical hole doping concentration for the antiferromagnetic transition is $n_h \approx 1.42 \times 10^{-2}$ hole per atom, which is larger than that of single-layer BPN. An interesting feature of hole-doped bilayer BPN is another magnetic phase transition from antiferromagnetic ordering to ferrimagnetic one at a higher hole doping concentration $n_h \approx 3.63 \times 10^{-2}$ hole per atom. In the ferrimagnetic state of bilayer BPN, each layer has ferrimagnetic ordering, where spins of rectangle clusters are aligned oppositely to those of dimers, which is the same as ferrimagnetic single-layer BPN. However, when considering spins at the same positions in the upper and lower layers, they are oriented in the same direction, as shown in Fig. 10(c).

Similar to hole-doped single-layer BPN, the magnetic transitions in hole-doped bilayer BPN are not associated with the full recovery of type-II Dirac points and saddle-shaped bands around Γ , as shown in Figs. 8(d)-(i). The type-II Dirac point is formed on the upper flat band on ΓX , while the lower flat band does not host a type-II Dirac point. For the ferrimagnetic state, energy bands associated with opposite spins are split, resulting in four flat bands on ΓX in Fig. 8(h).

3. Magnetic interactions

Given that the monolayer and bilayer of BPN are metallic, their magnetic behavior can be attributed to the Stoner-type magnetism of itinerant electrons in the metallic system⁷³⁻⁷⁸. As shown in the band structures, monolayer and bilayer of BPN have distinctive features in the electronic structure: nearly flat bands on ΓX and saddle-point vHSs at Γ and Y . These features contribute to an increased DOS that can lead to the Stoner-type magnetism of itinerant electrons. To investigate this, we calculate the DOS around E_F for monolayer and bilayer of BPN with uniaxial strains and hole doping⁷⁹.

As illustrated in Fig. 9, the DOS exhibits different behaviors when monolayer BPN under uniaxial strains and hole-doped monolayer are compared. When uniaxial strains ε_{xx} are applied, saddle points at Γ and Y move close to E_F , while the nearly flat band shifts away [See Figs. 9(a1)-(a3)]. As a result, the DOS near E_F primarily originates from the two saddle points as shown in Figs. 9(b1)-(b3). It is known that a saddle point of 2D band structures gives rise to the logarithmically divergent DOS⁸⁰. As seen in Figs. 9(b1)-(b3), the DOS exhibits two sharp peaks, whose energies correspond to the saddle points at Γ and Y . The peaks have long logarithmic tails. In contrast, hole-doped monolayer BPN shows enhanced DOS near E_F due to the nearly flat band on ΓX . Since this nearly flat band merges with the saddle point at Γ , the DOS peak at E_F has a logarithmic tail on the lower side of the DOS peak. For bilayer BPN, the contributions to the DOS, despite the doubled number of nearly flat bands and saddle points, are similar to monolayer BPN under uniaxial strains and hole doping.

Lastly, to explore magnetic interactions between magnetic moments, we perform constrained magnetization calculations⁸²⁻⁸⁴. In this calculation, we maintain the magnitude of magnetic moments, but opposite magnetic moments are flipped so that all magnetic moments are aligned in the same direction. As discussed before, monolayer BPN with an appropriate strain ε_{xx} and hole doping n_h displays ferrimagnetic ordering, where majority magnetic moments at the tetragon and minority ones at the dimer unit are aligned in opposite directions. For instance, the spin polarization density $\Delta\rho$ at $\varepsilon_{xx} = 5.6\%$ are depicted in Fig. 10(a). We denote E_{Ferro} as the total energy of the ferromagnetic ordering, where minority magnetic moments at the dimer are flipped in the constrained magnetization calculation. Comparing the total energy E_{Ferr} of the ferrimagnetic phase, we calculate the total energy difference $\Delta E = E_{\text{Ferr}} - E_{\text{Ferro}}$ as a function of x -strain ε_{xx} and hole doping n_h in Figs. 11(a) and (b). This calculation shows that the transition from the ferrimagnetic phase to the ferromagnetic one requires a positive energy cost, with a maximum of 25 (10) meV, depending on ε_{xx} (n_h).

In the case of bilayer BPN, each layer exhibits ferrimagnetic ordering similar to monolayer BPN. In the antiferromagnetic (AFM) phase of bilayer BPN, the lower

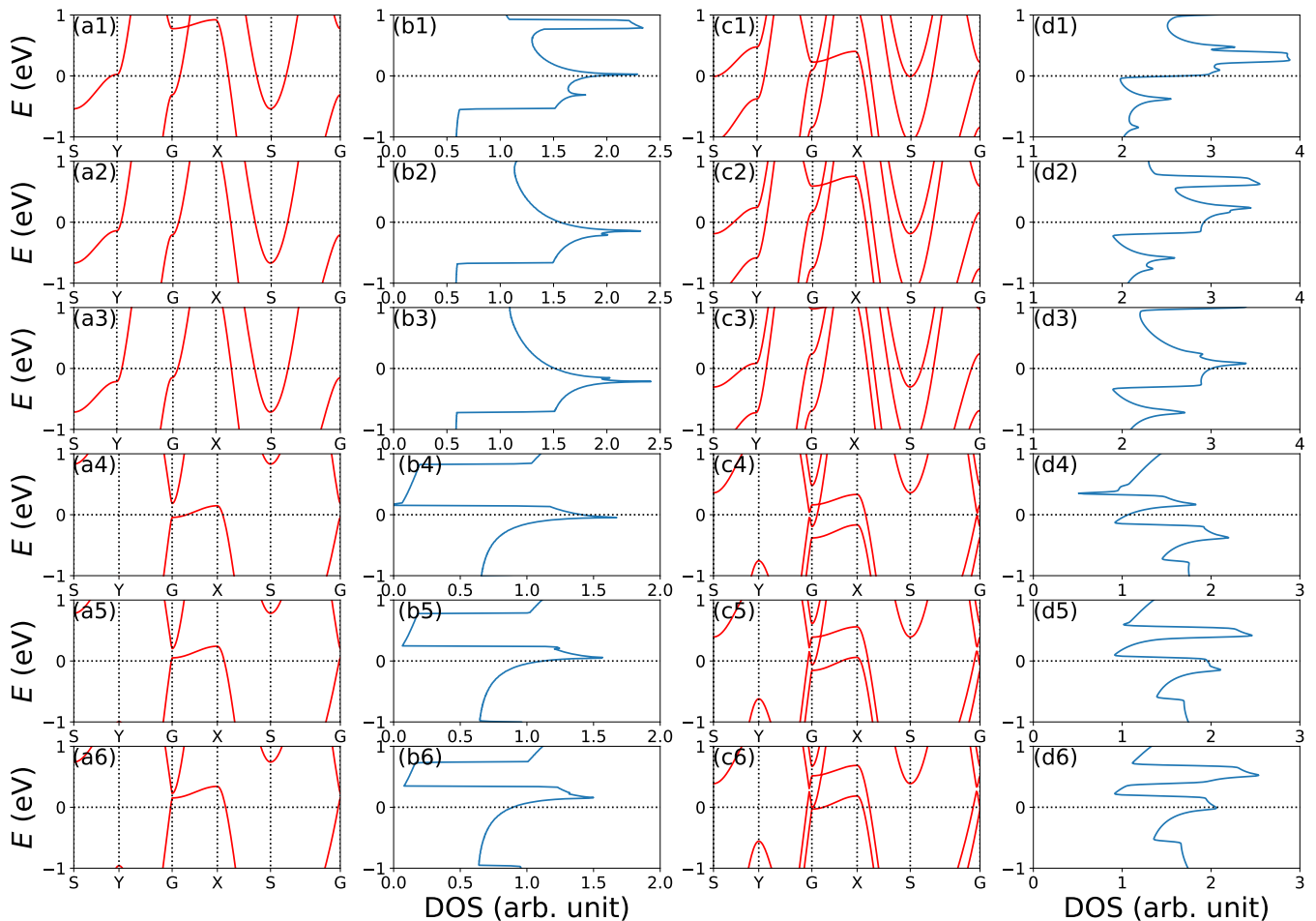


FIG. 9. (Color online) Band structures (the first column, blue solid lines) and corresponding DOS (the second column, red solid lines) for monolayer BPN with uniaxial strains and hole doping concentrations: (a1) and (b1) $\varepsilon_{xx} = 5.6\%$, (a2) and (b2) $\varepsilon_{xx} = 6.5\%$, (a3) and (b3) $\varepsilon_{xx} = 7.4\%$, (a4) and (b4) $n_h = 1.7 \times 10^{-2}$ hole/atom, (a5) and (b5) $n_h = 2.5 \times 10^{-2}$ hole/atom, and (a6) and (b6) $n_h = 3.3 \times 10^{-2}$ hole/atom. Band structures (the third column) and corresponding DOS (the fourth column) for bilayer BPN with uniaxial strains and hole doping concentrations: (c1) and (d1) $\varepsilon_{xx} = 4.7\%$, (c2) and (d2) $\varepsilon_{xx} = 6.5\%$, (c3) and (d3) $\varepsilon_{xx} = 7.8\%$, (c4) and (d4) $n_h = 1.7 \times 10^{-2}$ hole/atom, (c5) and (d5) $n_h = 2.9 \times 10^{-2}$ hole/atom, and (c6) and (d6) $n_h = 3.8 \times 10^{-2}$ hole/atom.

and upper layers display opposite magnetic moments, as depicted in Fig. 10(b). To be specific, the magnetic moments of the tetragon (dimer) unit in the lower layer have the same magnitude as those in the upper layer, but their directions are opposite. We perform constrained magnetization calculations where the magnetic moments of the tetragon (dimer) in the lower and the upper layers are aligned in the same direction and the ferrimagnetic ordering within each layer is fixed, which is referred to as the ferrimagnetic (FM) ordering of bilayer BPN. Denoting the resulting total energy as E_{FM} , Figs. 11(c) and (d) illustrate the total energy difference $\Delta E = E_{\text{AFM}} - E_{\text{FM}}$ for bilayer BPN under uniaxial strains ε_{xx} and hole doping. The flipping of interlayer magnetic moment from the antiferromagnetic phase to the ferrimagnetic one requires an energy cost, suggesting the stability of

the antiferromagnetic ordering in bilayer BPN. In the previous subsection, the highly hole-doped bilayer BPN ($n_h > 3.63 \times 10^{-2}$ hole per atom) exhibits ferrimagnetic ordering, as depicted in Fig. 10(c). In this case, we compute the total energy of the antiferromagnetic ordering in the constrained magnetization calculations, and compare E_{FM} and E_{AFM} as shown in Fig. 11(d). For the high hole-doping concentration, the calculation reveals that the ferrimagnetic ordering is energetically more favorable than the antiferromagnetic one, but their total energy difference is less than approximately 0.4 meV.

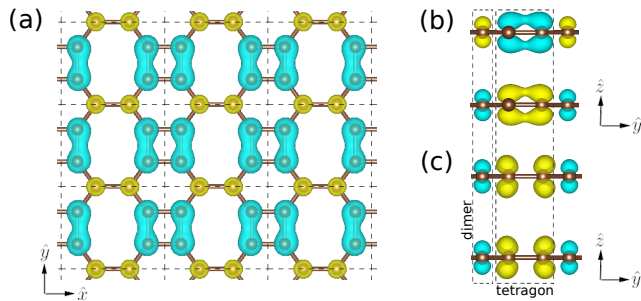


FIG. 10. (Color online) Spin polarization density distributions $\Delta\rho = \rho_{\uparrow} - \rho_{\downarrow}$. Cyan and yellow colors represent opposite spins. (a) Top view of spin polarization distribution for single-layer BPN under the x strain of 5.6 %. (b) Side view of antiferromagnetic spin polarization distribution when the hole doping is 2.5×10^{-2} hole/atom. (c) Side view of ferrimagnetic spin polarization distribution when the hole doping is 4×10^{-2} hole/atom. Density distributions are drawn by VESTA⁸¹

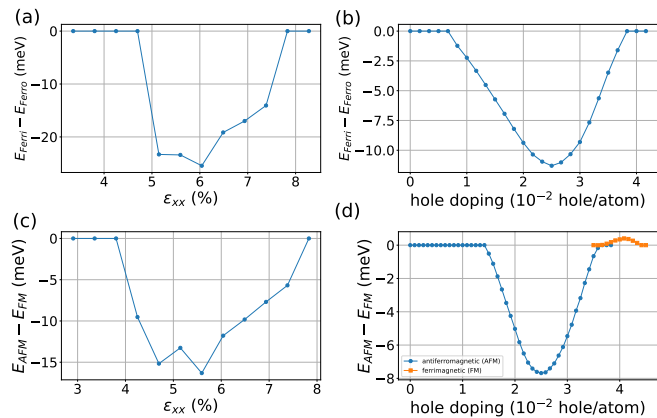


FIG. 11. (Color online) Total energy differences between two magnetic phases of monolayer and bilayer BPN: $E_{\text{Ferri}} - E_{\text{Ferro}}$ of monolayer BPN as a function of (a) uniaxial strains ε_{xx} and (b) hole doping concentrations n_h . $E_{\text{AFM}} - E_{\text{FM}}$ of bilayer BPN varying (c) ε_{xx} and (d) n_h .

IV. CONCLUSIONS

In this study, we examined the magnetic transitions of monolayer and bilayer BPN, under the influence of external perturbations such as uniaxial strains and hole doping. To account for electron correlations, we employed the DFT+ U + V method, which incorporates on-site and inter-site interactions as extended Hubbard corrections. These extended Hubbard corrections were consistently applied throughout all DFT calculations, encompassing structure relaxations and electronic band structure calculations.

Our findings indicate that both the BPN monolayer and bilayer, in their fully relaxed structures, exhibit non-magnetic behavior. However, the application of uniaxial strains along the dimer unit direction induces a ferrimagnetic transition in the monolayer, whereas the bilayer experiences a magnetic transition towards an antiferromagnetic phase.

Furthermore, we explored an alternative approach for inducing magnetic transitions in BPN monolayer and bilayer through hole doping. At a moderate level of hole doping, the monolayer assumes a ferrimagnetic phase, while the bilayer adopts an anti-ferrimagnetic state. At increased hole doping levels, the bilayer demonstrates the potential for transitioning into a ferrimagnetic phase. These results offer valuable insights into the intriguing magnetic behavior of BPN-based structures and open up avenues for further investigations in this field.

CONFLICTS OF INTEREST

There are no conflicts to declare.

ACKNOWLEDGEMENTS

We thank Jeongwoo Kim, Davide Ceresoli, and Young-Woo Son for fruitful discussions and critical reading. This work was supported by the National Research Foundation of Korea (NRF) grant funded by the Korea government (Grant No. NRF-2022R1F1A1074670) and by the Open KIAS Center at Korea Institute for Advanced Study.

* sejoong@alum.mit.edu

¹ Qitang Fan, Linghao Yan, Matthias W. Tripp, Ondřej Krejčí, Stavrina Dimosthenous, Stefan R. Kachel, Mengyi Chen, Adam S. Foster, Ulrich Koert, Peter Liljeroth, and J. Michael Gottfried, “Biphenylene network: A nonbenzenoid carbon allotrope,” *Science* **372**, 852–856 (2021).

² A. H. Castro Neto, F. Guinea, N. M. R. Peres, K. S. Novoselov, and A. K. Geim, “The electronic properties of graphene,” *Rev. Mod. Phys.* **81**, 109–162 (2009).

³ Young-Woo Son, Hosub Jin, and Sejoong Kim, “Magnetic ordering, anomalous Lifshitz transition, and topological grain boundaries in two-dimensional biphenylene network,” *Nano Letters* **22**, 3112–3117 (2022).

⁴ Peng-Fei Liu, Jingyu Li, Chi Zhang, Xin-Hai Tu, Junrong Zhang, Ping Zhang, Bao-Tian Wang, and David J. Singh, “Type-II Dirac cones and electron-phonon interaction in monolayer biphenylene from first-principles calculations,” *Phys. Rev. B* **104**, 235422 (2021).

- ⁵ Ke Wang, Kai Ren, Dingbo Zhang, Yuan Cheng, and Gang Zhang, "Phonon properties of biphenylene monolayer by first-principles calculations," *Applied Physics Letters* **121**, 042203 (2022).
- ⁶ Amin Hamed Mashhadzadeh, Maryam Zarghami Dehaghani, Fatemeh Molaie, Sasan Fooladapanjeh, Omid Farzadian, and Christos Spitas, "A theoretical insight into the mechanical properties and phonon thermal conductivity of biphenylene network structure," *Computational Materials Science* **214**, 111761 (2022).
- ⁷ Bohayra Mortazavi and Alexander V. Shapeev, "Anisotropic mechanical response, high negative thermal expansion, and outstanding dynamical stability of biphenylene monolayer revealed by machine-learning interatomic potentials," *FlatChem* **32**, 100347 (2022).
- ⁸ M. L. Pereira, W. F. da Cunha, R. T. de Sousa, G. D. Amvame Nze, D. S. Galvão, and L. A. Ribeiro, "On the mechanical properties and fracture patterns of the non-benzenoid carbon allotrope (biphenylene network): a reactive molecular dynamics study," *Nanoscale* **14**, 3200–3211 (2022).
- ⁹ Xiaoqiong Ren, Ke Wang, Yue Yu, Daokun Zhang, Gang Zhang, and Yuan Cheng, "Tuning the mechanical anisotropy of biphenylene by boron and nitrogen doping," *Computational Materials Science* **222**, 112119 (2023).
- ¹⁰ Salih Demirci, Şafak Çalhoğlu, Taylan Görkan, Ethem Aktürk, and Salim Ciraci, "Stability and electronic properties of monolayer and multilayer structures of group-IV elements and compounds of complementary groups in biphenylene network," *Phys. Rev. B* **105**, 035408 (2022).
- ¹¹ Yi Luo, Chongdan Ren, Yujing Xu, Jin Yu, Sake Wang, and Minglei Sun, "A first principles investigation on the structural, mechanical, electronic, and catalytic properties of biphenylene," *Scientific Reports* **11**, 19008 (2021).
- ¹² A Bafekry, M Faraji, M M Fadlallah, H R Jappor, S Karbasizadeh, M Ghergherehchi, and D Gogova, "Biphenylene monolayer as a two-dimensional nonbenzenoid carbon allotrope: a first-principles study," *Journal of Physics: Condensed Matter* **34**, 015001 (2021).
- ¹³ Pavel Rublev, Nikolay V. Tkachenko, and Alexander I. Boldyrev, "Overlapping electron density and the global delocalization of π -aromatic fragments as the reason of conductivity of the biphenylene network," *Journal of Computational Chemistry* **44**, 168–178 (2023).
- ¹⁴ Guogang Liu, Tong Chen, Xiaohui Li, Zhonghui Xu, and Xianbo Xiao, "Electronic transport in biphenylene network monolayer: Proposals for 2D multifunctional carbon-based nanodevices," *Applied Surface Science* **599**, 153993 (2022).
- ¹⁵ Suman Chowdhury, Supriya Ghosal, Deep Mondal, and Debnarayan Jana, "First-principles and machine-learning study of electronic and phonon transport in carbon-based AA-stacked bilayer biphenylene nanosheets," *Journal of Physics and Chemistry of Solids* **170**, 110909 (2022).
- ¹⁶ Taylan Gorkan, Şafak Çalhoğlu, Salih Demirci, Ethem Aktürk, and Salim Ciraci, "Functional carbon and silicon monolayers in biphenylene network," *ACS Applied Electronic Materials* **4**, 3056–3070 (2022).
- ¹⁷ Isaac Alcón, Gaetano Calogero, Nick Papior, Aleandro Antidormi, Kenan Song, Aron W. Cummings, Mads Brandbyge, and Stephan Roche, "Unveiling the multiradical character of the biphenylene network and its anisotropic charge transport," *Journal of the American Chemical Society* **144**, 8278–8285 (2022), pMID: 35476458.
- ¹⁸ Hong Shen, Riye Yang, Kun Xie, Zhiyuan Yu, Yuxiang Zheng, Rongjun Zhang, Liangyao Chen, Bi-Ru Wu, Wan-Sheng Su, and Songyou Wang, "Electronic and optical properties of hydrogen-terminated biphenylene nanoribbons: a first-principles study," *Phys. Chem. Chem. Phys.* **24**, 357–365 (2022).
- ¹⁹ Yunhao Xie, Liang Chen, Jing Xu, and Wei Liu, "Effective regulation of the electronic properties of a biphenylene network by hydrogenation and halogenation," *RSC Adv.* **12**, 20088–20095 (2022).
- ²⁰ Ningjing Yang, Qingyuan Chen, Yafang Xu, Jinlong Luo, Hai Yang, and Guojun Jin, "Strain-modulated electronic transport in two-dimensional carbon allotropes," *AIP Advances* **12**, 045102 (2022).
- ²¹ Lin Zhang and Peiqing Tong, "Even-odd chain dependent spin valve effect on a zigzag biphenylene nanoribbon junction," *Journal of Physics: Condensed Matter* **34**, 395301 (2022).
- ²² Kai Ren, Huabing Shu, Wenyi Huo, Zhen Cui, and Yujing Xu, "Tuning electronic, magnetic and catalytic behaviors of biphenylene network by atomic doping," *Nanotechnology* **33**, 345701 (2022).
- ²³ Yanfeng Ge, Zhicui Wang, Xing Wang, Wenhui Wan, and Yong Liu, "Superconductivity in the two-dimensional non-benzenoid biphenylene sheet with Dirac cone," *2D Materials* **9**, 015035 (2021).
- ²⁴ Guo-Hua Liu, Liu Yang, Shu-Xiang Qiao, Na Jiao, Ying-Jie Chen, Mei-Yan Ni, Meng-Meng Zheng, Hong-Yan Lu, and Ping Zhang, "Superconductivity of monolayer functionalized biphenylene with Dirac cones," *Phys. Chem. Chem. Phys.* **25**, 2875–2881 (2023).
- ²⁵ Harish P. Veeravenkata and Ankit Jain, "Density functional theory driven phononic thermal conductivity prediction of biphenylene: A comparison with graphene," *Carbon* **183**, 893–898 (2021).
- ²⁶ Pei Zhang, Tao Ouyang, Chao Tang, Chaoyu He, Jin Li, Chunxiao Zhang, Ming Hu, and Jianxin Zhong, "The intrinsic thermal transport properties of the biphenylene network and the influence of hydrogenation: a first-principles study," *J. Mater. Chem. C* **9**, 16945–16951 (2021).
- ²⁷ Zhen Tong, Alessandro Pecchia, ChiYung Yam, Traian Dumitrică, and Thomas Frauenheim, "Ultrahigh electron thermal conductivity in T-graphene, biphenylene, and net-graphene," *Advanced Energy Materials* **12**, 2200657 (2022).
- ²⁸ Qingfang Li, Jian Zhou, Gang Liu, and X.G. Wan, "Extraordinary negative thermal expansion of monolayer biphenylene," *Carbon* **187**, 349–353 (2022).
- ²⁹ Zhong-Xiang Xie, Xue-Kun Chen, Xia Yu, Yuan-Xiang Deng, Yong Zhang, Wu-Xing Zhou, and Pin-Zhen Jia, "Intrinsic thermoelectric properties in biphenylene nanoribbons and effect of lattice defects," *Computational Materials Science* **220**, 112041 (2023).
- ³⁰ Guangyu Yang, Yanxiao Hu, Zhanjun Qiu, Bo-Lin Li, Ping Zhou, Dengfeng Li, and Gang Zhang, "Abnormal strain-dependent thermal conductivity in biphenylene monolayer using machine learning interatomic potential," *Applied Physics Letters* **122**, 082202 (2023).
- ³¹ Tianyang Liu, Yu Jing, and Yafei Li, "Two-dimensional biphenylene: A graphene allotrope with superior activity toward electrochemical oxygen reduction reaction," *The Journal of Physical Chemistry Letters* **12**, 12230–12234 (2021), pMID: 34928622.

- ³² Pratap Mane, Surinder Pal Kaur, and Brahmananda Chakraborty, “Enhanced reversible hydrogen storage efficiency of zirconium-decorated biphenylene monolayer: A computational study,” *Energy Storage* **4**, e377 (2022).
- ³³ Lida Asadi, Zohreh Saadati, and Mahboobeh Salehpour, “Theoretical evaluation of Al-doped biphenylene nanosheet sensing properties toward gamma-butyrolactone,” *Structural Chemistry* **33**, 1947–1955 (2022).
- ³⁴ Wan-Sheng Su and Chen-Hao Yeh, “Theoretical investigation of methane oxidation reaction over a novel metal-free catalyst biphenylene network,” *Diamond and Related Materials* **124**, 108897 (2022).
- ³⁵ Hiba Khaled Al-Jayyousi, Muhammad Sajjad, Kin Liao, and Nirpendra Singh, “Two-dimensional biphenylene: a promising anchoring material for lithium-sulfur batteries,” *Scientific Reports* **12**, 4653 (2022).
- ³⁶ Ting Han, Yu Liu, Xiaodong Lv, and Fengyu Li, “Biphenylene monolayer: a novel nonbenzenoid carbon allotrope with potential application as an anode material for high-performance sodium-ion batteries,” *Phys. Chem. Chem. Phys.* **24**, 10712–10716 (2022).
- ³⁷ Xin-Wei Chen, Zheng-Zhe Lin, and Xi-Mei Li, “Biphenylene network as sodium ion battery anode material,” *Phys. Chem. Chem. Phys.* **25**, 4340–4348 (2023).
- ³⁸ Kaifeng Niu, Qitang Fan, Lifeng Chi, Johanna Rosen, J. Michael Gottfried, and Jonas Björk, “Unveiling the formation mechanism of the biphenylene network,” *Nanoscale Horiz.* **8**, 368–376 (2023).
- ³⁹ Alexey A. Soluyanov, Dominik Gresch, Zhijun Wang, QuanSheng Wu, Matthias Troyer, Xi Dai, and B. Andrei Bernevig, “Type-II Weyl semimetals,” *Nature* **527**, 495–498 (2015).
- ⁴⁰ Er-jun Kan, Zhenyu Li, Jinlong Yang, and J. G. Hou, “Half-metallicity in edge-modified zigzag graphene nanoribbons,” *Journal of the American Chemical Society* **130**, 4224–4225 (2008).
- ⁴¹ Young-Woo Son, Marvin L. Cohen, and Steven G. Louie, “Half-metallic graphene nanoribbons,” *Nature* **444**, 347–349 (2006).
- ⁴² J. Jung, T. Pereg-Barnea, and A. H. MacDonald, “Theory of interedge superexchange in zigzag edge magnetism,” *Phys. Rev. Lett.* **102**, 227205 (2009).
- ⁴³ P. O. Lehtinen, A. S. Foster, Yuchen Ma, A. V. Krasheninnikov, and R. M. Nieminen, “Irradiation-induced magnetism in graphite: A density functional study,” *Phys. Rev. Lett.* **93**, 187202 (2004).
- ⁴⁴ Oleg V. Yazyev and Lothar Helm, “Defect-induced magnetism in graphene,” *Phys. Rev. B* **75**, 125408 (2007).
- ⁴⁵ Alex Yong Sheng Eng, Hwee Ling Poh, Filip Šaněk, Miroslav Maryško, Stanislava Matějková, Zdeněk Sofer, and Martin Pumera, “Searching for magnetism in hydrogenated graphene: Using highly hydrogenated graphene prepared via birch reduction of graphite oxides,” *ACS Nano* **7**, 5930–5939 (2013).
- ⁴⁶ J. Zhou, Q. Wang, Q. Sun, X. S. Chen, Y. Kawazoe, and P. Jena, “Ferromagnetism in semihydrogenated graphene sheet,” *Nano Letters* **9**, 3867–3870 (2009).
- ⁴⁷ Lanfei Xie, Xiao Wang, Jiong Lu, Zhenhua Ni, Zhiqiang Luo, Hongying Mao, Rui Wang, Yingying Wang, Han Huang, Dongchen Qi, Rong Liu, Ting Yu, Zexiang Shen, Tom Wu, Haiyang Peng, Barbaros Özyilmaz, Kianping Loh, Andrew T. S. Wee, Ariando, and Wei Chen, “Room temperature ferromagnetism in partially hydrogenated epitaxial graphene,” *Applied Physics Letters* **98**, 193113 (2011).
- ⁴⁸ P. O. Lehtinen, A. S. Foster, A. Ayuela, A. Krasheninnikov, K. Nordlund, and R. M. Nieminen, “Magnetic properties and diffusion of adatoms on a graphene sheet,” *Phys. Rev. Lett.* **91**, 017202 (2003).
- ⁴⁹ Yan Gao, Xiaolong Feng, Ben-Chao Gong, Chengyong Zhong, Shengyuan A. Yang, Kai Liu, and Zhong-Yi Lu, “Theoretical design of all-carbon networks with intrinsic magnetism,” *Carbon* **177**, 11–18 (2021).
- ⁵⁰ Vivaldo Leiria Campo and Matteo Cococcioni, “Extended DFT + U + V method with on-site and inter-site electronic interactions,” *Journal of Physics: Condensed Matter* **22**, 055602 (2010).
- ⁵¹ Iurii Timrov, Nicola Marzari, and Matteo Cococcioni, “Self-consistent hubbard parameters from density-functional perturbation theory in the ultrasoft and projector-augmented wave formulations,” *Phys. Rev. B* **103**, 045141 (2021).
- ⁵² Iurii Timrov, Nicola Marzari, and Matteo Cococcioni, “Hubbard parameters from density-functional perturbation theory,” *Phys. Rev. B* **98**, 085127 (2018).
- ⁵³ Ruchika Mahajan, Iurii Timrov, Nicola Marzari, and Arti Kashyap, “Importance of intersite hubbard interactions in β -mno₂: A first-principles DFT + U + V study,” *Phys. Rev. Mater.* **5**, 104402 (2021).
- ⁵⁴ Sang-Hoon Lee and Young-Woo Son, “First-principles approach with a pseudohybrid density functional for extended hubbard interactions,” *Phys. Rev. Res.* **2**, 043410 (2020).
- ⁵⁵ Nicolas Tancogne-Dejean and Angel Rubio, “Parameter-free hybridlike functional based on an extended hubbard model: DFT + U + V,” *Phys. Rev. B* **102**, 155117 (2020).
- ⁵⁶ Lars Hedin, “New method for calculating the one-particle green’s function with application to the electron-gas problem,” *Phys. Rev.* **139**, A796–A823 (1965).
- ⁵⁷ Woil Yang, Seung-Hoon Jhi, Sang-Hoon Lee, and Young-Woo Son, “Ab initio study of lattice dynamics of group iv semiconductors using pseudohybrid functionals for extended hubbard interactions,” *Phys. Rev. B* **104**, 104313 (2021).
- ⁵⁸ Woil Yang, Bo Gyu Jang, Young-Woo Son, and Seung-Hoon Jhi, “Lattice dynamical properties of antiferromagnetic oxides calculated using self-consistent extended Hubbard functional method,” *Journal of Physics: Condensed Matter* **34**, 295601 (2022).
- ⁵⁹ Bo Gyu Jang, Minjae Kim, Sang-Hoon Lee, Woil Yang, Seung-Hoon Jhi, and Young-Woo Son, “Intersite Coulomb interactions in charge-ordered systems,” *Phys. Rev. Lett.* **130**, 136401 (2023).
- ⁶⁰ Anton Kokalj, “Xcrysden—a new program for displaying crystalline structures and electron densities,” *Journal of Molecular Graphics and Modelling* **17**, 176–179 (1999).
- ⁶¹ P. Giannozzi, O. Andreussi, T. Brumme, O. Bunau, M. Buongiorno Nardelli, M. Calandra, R. Car, C. Cavazzoni, D. Ceresoli, M. Cococcioni, N. Colonna, I. Carnimeo, A. Dal Corso, S. de Gironcoli, P. Delugas, R. A. DiStasio Jr, A. Ferretti, A. Floris, G. Fratesi, G. Fugallo, R. Gebauer, U. Gerstmann, F. Giustino, T. Gorni, J. Jia, M. Kawamura, H.-Y. Ko, A. Kokalj, E. Küçükbenli, M. Lazzeri, M. Marsili, N. Marzari, F. Mauri, N. L. Nguyen, H.-V. Nguyen, A. Otero de-la Roza, L. Paulatto, S. Poncé, D. Rocca, R. Sabatini, B. Santra, M. Schlipf, A. P. Seitsonen, A. Smogunov, I. Timrov, T. Thon-

- hauser, P. Umari, N. Vast, X. Wu, and S. Baroni, “Quantum ESPRESSO: a modular and open-source software project for quantum simulations of materials,” *J. Phys.: Condens. Matter* **21**, 395502 (2009).
- ⁶² P. Giannozzi, S. Baroni, N. Bonini, M. Calandra, R. Car, C. Cavazzoni, D. Ceresoli, G. L. Chiarotti, M. Cococcioni, I. Dabo and A. Dal Corso, S. Fabris, G. Fratesi, S. de Gironcoli, R. Gebauer, U. Gerstmann, C. Gougousis, A. Kokalj, M. Lazzeri, L. Martin-Samos, N. Marzari, F. Mauri, R. Mazzarello, S. Paolini, A. Pasquarello, L. Paulatto, C. Sbraccia, S. Scandolo, G. Sclauzero, A. P. Seitsonen, A. Smogunov, P. Umari, and R. M. Wentzcovitch, “Advanced capabilities for materials modelling with Quantum ESPRESSO,” *J. Phys.: Condens. Matter* **29**, 465901 (2017).
- ⁶³ J. P. Perdew, K. Burke, and M. Ernzerhof, “Generalized gradient approximation made simple,” *Phys. Rev. Lett.* **77**, 3865 (1996).
- ⁶⁴ D. R. Hamann, “Optimized norm-conserving vanderbilt pseudopotentials,” *Phys. Rev. B* **88**, 085117 (2013).
- ⁶⁵ M. J. van Setten, M. Giantomassi, E. Bousquet, M. J. Verstraete, D. R. Hamann, X. Gonze, and G.-M. Rignanese, “The pseudodojo: Training and grading a 85 element optimized norm-conserving pseudopotential table,” *Comput. Phys. Commun.* **226**, 39–54 (2018).
- ⁶⁶ Ikutaro Hamada, “van der waals density functional made accurate,” *Phys. Rev. B* **89**, 121103 (2014).
- ⁶⁷ Hyun-Jung Kim, Seoung-Hun Kang, Ikutaro Hamada, and Young-Woo Son, “Origins of the structural phase transitions in mTe_2 and wTe_2 ,” *Phys. Rev. B* **95**, 180101 (2017).
- ⁶⁸ Luis A. Agapito, Stefano Curtarolo, and Marco Buongiorno Nardelli, “Reformulation of DFT+ u as a pseudohybrid hubbard density functional for accelerated materials discovery,” *Phys. Rev. X* **5**, 011006 (2015).
- ⁶⁹ Mingzhe Yan, Huaqing Huang, Kenan Zhang, Eryin Wang, Wei Yao, Ke Deng, Guoliang Wan, Hongyun Zhang, Masashi Arita, Haitao Yang, Zhe Sun, Hong Yao, Yang Wu, Shoushan Fan, Wenhui Duan, and Shuyun Zhou, “Lorentz-violating type-II Dirac fermions in transition metal dichalcogenide PtTe_2 ,” *Nature Communications* **8**, 257 (2017).
- ⁷⁰ N. P. Armitage, E. J. Mele, and Ashvin Vishwanath, “Weyl and Dirac semimetals in three-dimensional solids,” *Rev. Mod. Phys.* **90**, 015001 (2018).
- ⁷¹ Fucong Fei, Xiangyan Bo, Rui Wang, Bin Wu, Juan Jiang, Dongzhi Fu, Ming Gao, Hao Zheng, Yulin Chen, Xuefeng Wang, Haijun Bu, Fengqi Song, Xiangang Wan, Baigeng Wang, and Guanghou Wang, “Nontrivial Berry phase and type-II Dirac transport in the layered material PdTe_2 ,” *Phys. Rev. B* **96**, 041201 (2017).
- ⁷² Han-Jin Noh, Jinwon Jeong, En-Jin Cho, Kyoo Kim, B. I. Min, and Byeong-Gyu Park, “Experimental realization of type-II Dirac fermions in a PdTe_2 superconductor,” *Phys. Rev. Lett.* **119**, 016401 (2017).
- ⁷³ E. C. Stoner, “Collective electron ferromagnetism,” *Proc. R. Soc. Lond. A* **165**, 372–414 (1938).
- ⁷⁴ A B Lidiard, “Antiferromagnetism in metals,” *Proceedings of the Physical Society. Section A* **66**, 1188 (1953).
- ⁷⁵ A. B. Lidiard and Charles Alfred Coulson, “Antiferromagnetism in metals,” *Proceedings of the Royal Society of London. Series A. Mathematical and Physical Sciences* **224**, 161–176 (1954).
- ⁷⁶ R H Tredgold, “On antiferromagnetism in metals,” *Proceedings of the Physical Society. Section A* **67**, 1018 (1954).
- ⁷⁷ T. M. Rice, “Band-structure effects in itinerant antiferromagnetism,” *Phys. Rev. B* **2**, 3619–3630 (1970).
- ⁷⁸ M. Shimizu, “Theory of itinerant electron antiferromagnetism,” *Journal of Magnetism and Magnetic Materials* **45**, 144–150 (1984).
- ⁷⁹ Jonathan R. Yates, Xinjie Wang, David Vanderbilt, and Ivo Souza, “Spectral and fermi surface properties from wannier interpolation,” *Phys. Rev. B* **75**, 195121 (2007).
- ⁸⁰ T. M. Rice and G. K. Scott, “New mechanism for a charge-density-wave instability,” *Phys. Rev. Lett.* **35**, 120–123 (1975).
- ⁸¹ Koichi Momma and Fujio Izumi, “*VESTA* for three-dimensional visualization of crystal, volumetric and morphology data,” *Journal of Applied Crystallography* **44**, 1272–1276 (2011).
- ⁸² Hongjun Xiang, Changhoon Lee, Hyun-Joo Koo, Xingao Gong, and Myung-Hwan Whangbo, “Magnetic properties and energy-mapping analysis,” *Dalton Trans.* **42**, 823–853 (2013).
- ⁸³ H. J. Xiang, E. J. Kan, Su-Huai Wei, M.-H. Whangbo, and X. G. Gong, “Predicting the spin-lattice order of frustrated systems from first principles,” *Phys. Rev. B* **84**, 224429 (2011).
- ⁸⁴ Jeonghoon Hong, Chang-Jong Kang, and Jeongwoo Kim, “Role of electronic correlations in room-temperature ferromagnetism of monolayer MnSe_2 ,” *Phys. Rev. B* **106**, 195428 (2022).